Corrosion Behavior of Solution-Annealed CoCrMo Medical Implant Alloys

Pooja Panigrahi
Advisor: Laurence D. Marks
Mentor: Yifeng Liao
MSE 396-2 Instructor: Kathleen Stair
Department of Materials Science and Engineering
The McCormick School of Engineering and Applied Sciences
Northwestern University
June 6, 2011

Corrosion Behavior of Solution-Annealed CoCrMo Medical Implant Alloys

Pooja Panigrahi

Department of Materials Science and Engineering
The McCormick School of Engineering and Applied Sciences
Northwestern University
June 6, 2011

Abstract

Corrosion behavior of solution annealed high-carbon and low-carbon CoCrMo wrought alloy, commonly used in medical joint implants, was investigated. The surface passivation properties remained similar with and without the various solution anneal conditions, while the rate of corrosion was lower for solution annealed high-carbon CoCrMo. Corrosion was found to target phase boundaries and certain grain boundaries in the high-carbon alloy. This preferential corrosion may be due to chromium depletion at the boundaries, higher grain boundary energy as a function of the misorientation angle between the neighboring grains, or both. These findings suggest that solution annealing the high-carbon CoCrMo alloys may lower the implant's rate of corrosion *in vivo* due to the more corrosion-resistant microstructure.

Table of Contents

1 - Introduction

A variety of conditions, most notably osteoarthritis and rheumatoid arthritis, may result in a patient's need for prosthetic joint implants at hips and knees. Every year, as patients live longer, demand is rising with and increasing number of diagnoses [1]. CoCrMo alloys are currently the leading materials for metal-on-metal implant bearings. These alloys have a superior combination of properties including fracture toughness, ductility, biocompatibility, strength, and corrosion resistance compared to UHMWPE, alumina, titanium alloys, and combined ceramic, metal, and polyethylene systems [2].

Despite the superior mechanical performance of the CoCrMo alloys, elevated levels of cobalt and chromium cations have frequently been detected in the blood of patients with implants comprised of this material [3]. These ions result from corrosion of the alloys. Chromium and cobalt cations are known to form metal-protein complexes *in vivo*, and these antigens elicit the hypersensitivity responses such as dermatitis, urticarial vasculitis, metallosis, muscular necrosis, and a variety of other mild to severe medical conditions [4].

Metal implant corrosion is controlled by both the thermodynamic driving forces of the redox reactions which cause corrosion and the physical barriers which limit the kinetics of corrosion [2]. There is both a chemical driving force for oxidation and an electrical driving force for separating the positive (metal cation) and negative (electron) charges from one another during corrosion [2]. In the CoCrMo alloy system, the surface barrier limiting the kinetics of corrosion is in the form of a passive oxide film [2]. The formation and thickness of this chromium oxide film depend on the electric field across the oxide, since reduction and oxidation processes occur as necessary to keep the electric

field strength constant [2]. It is generally accepted that *in vivo*, the Cr_2O_3 passive film is 2-8 nm in thickness [5].

The bulk microstructure and solution annealing properties of CoCrMo alloys are well documented. The high-carbon alloys used in surgical implants consist predominantly of a γCo FCC matrix phase [6, 7], with nanograin precipitates [8] of mixed σ intermetallic (Cr_8Co_7) [7] and hard carbide phases to increase strength [6, 9]. At solutionizing temperatures above 1150°C and below incipient melting temperatures of about 1250°C [9], researchers achieved varying amounts of second phase dissolution [6, 9, 10]. The low-carbon alloys consist of the same matrix phase with no precipitate phases [11]. As with all wrought alloys, solution anneal heat treatments for both low-carbon and high-carbon CoCrMo are known to lead to grain coarsening.

While the thermal behavior of CoCrMo alloys has been explored thoroughly and the phases have been well characterized, very little is known about any differences in corrosion behavior that these microstructural changes may cause. Here, the corrosion properties of solution annealed CoCrMo wrought alloys are investigated.

2 - Methods and Materials

Twenty cylindrical wrought CoCrMo alloy pins, 12 mm in diameter and 7 mm thick, were obtained from the Rush University Orthopedics Center. Fifteen pins were of high-carbon (HC) content and five pins were of low-carbon (LC) content, Co-27.63Cr-6.04Mo-0.7Mn-0.66Si-0.241C-0.18Ni-0.14Fe (wt%) and Co-27.56Cr-5.7Mo-0.6Mn-0.55Ni-0.38Si-0.19Fe-0.034C (wt%) respectively. Experimental conditions consisted of solution heat treatments at 1150°C or 1230°C, for 2 or 24 hours, with no replicates (n=1)

for LC and three replicates (n=3) for HC. The low-carbon samples were included only for general comparison, but it is generally accepted that LC CoCrMo alloys have both poorer wear and corrosion resistance. Experimental conditions and replicates are summarized in Table 1. All heat treatments were performed in a box furnace in an air atmosphere, and surface oxides were removed mechanically using SiC grinding paper.

Table 1. Solution anneal heat treatments performed on CoCrMo samples

Samples	Temperature (^oC)	Time Annealed (h)
1 LC, 3 HC	-	-
1 LC, 3 HC	1150	2
1 LC, 3 HC	1150	24
1 LC, 3 HC	1230	2
1 LC, 3 HC	1230	24

Specimens were prepared for microstructural characterization using a mechanical polishing sequence of 9 μm, 3 μm, and 1 μm polycrystalline water-based colloidal abrasive solutions on Texmet polishing cloths. Specimens were then etched by a 2-5 minute immersion in a solution of 50 mL H_2O and 50 mL HCl with 4 g of $K_2S_5O_5$ as a reagent. A Hitachi S3400 SEM was used to obtain micrographs of specimens before and after electrochemical corrosion, using both secondary electron (SE) and backscattered electron (BSE) detectors. An accelerating voltage of 20 kV was used with a probe current of 70 μA.

After initial microstructural characterization, the surfaces of the samples were ground and re-polished to a mirror finish in preparation for corrosion testing. A Zygo white light interferometer (20x Mirau objective lens) was used to topographically image the exposed surfaces prior to corrosion to ensure acceptable average surface roughness

values (less than 50 nm). Each sample was then incorporated into a 4-chamber electrochemical cell as the working electrode (WE) with a graphite counter electrode (CE) and SCL reference electrode, all connected to a potentiostat and PC with the Gamry Electrochemical Analysis software. The corrosion cell was filled with 10 mL of bovine calf serum (BCS) buffered to a basic pH 7.4 solution, and placed in a hot water bath maintained at 37°C.

For each sample, the sequence of electrochemical tests began with a brief open circuit potential test (OCP1) to ensure the circuit was set up correctly. A potentiostatic test was then run, applying a constant cathodic potential to remove the passive film and any proteins that may have adsorbed on the metallic surface [12], so that all samples would have the same "starting point". A longer open circuit potential test (OCP2) was run before any corrosion was performed to determine the material's E_{oc}.

An electrochemical impedance spectroscopy (EIS) test was conducted to measure impedance as a function of frequency. Results from this test were used to construct Bode phase, Bode impedance, and Nyquist plots to qualitatively compare corrosion behavior. These results were also used to construct equivalent circuits (ECs), modeling the electrochemical system with a purely electrical circuit. For the ECs, a Randall's circuit of a solution resistance R_u in series with a polarization resistance R_p and capacitance C_f in parallel was used to model the properties of the electrolyte and the metal interface.

A potentiodynamic (cyclic polarization) test was performed to corrode the sample and measure the current at each applied potential. The resulting potentiodynamic curves were used to qualitatively compare the corrosion kinetics as they relate to the passive film. The corrosion potential E_{corr} and the current density i_{corr} at this potential were

approximated using the Tafel method. Lastly, another extended open circuit potential test (OCP3) was performed to measure the open circuit voltage E_{oc} of the corroded sample surface. Parameters for each test in this sequence are detailed in Table 2.

Table 2. Electrochemical corrosion testing sequence and parameters

Test	Parameter	Value
OCP1	Total time (s)	180
	Stability (mV/s)	0
	Sample period (s)	0.1
OCP2	Total time (s)	1800
	Stability (mV/s)	0
	Sample period (s)	0.1
Potentiostatic	Initial E (V) vs. E_{ref}	-0.9
	Initial time (s)	600
	Final E (V)	-0.9
	Final time (s)	0
	Sample period (s)	1
	Limit I (mA/cm^2)	25
	Open circuit E (V)	-0.232233
EIS	DC Voltage (V) vs. E_{oc}	0
	AC Voltage (mV ms)	10
	Initial frequency (Hz)	100000
	Final frequency (Hz)	0.005
	Points/decade	10
	Open circuit E (V)	-0.367033
Cyclic Polarization (Potentiodynamic)	Initial E (V) vs. E_{ref}	-0.8
	Apex E (V) vs. E_{ref}	1.8
	Final E (V) vs. E_{ref}	-0.8
	Forward scan (mV/s)	2
	Sample period (s)	0.5
	Reverse scan (mV/s)	2
	Apex I (mA/cm^2)	25
	Open circuit E (V)	-0.367033
OCP3	Total time (s)	1800
	Stability (mV/s)	0
	Sample period (s)	0.1

After corrosion testing, samples were removed and all components in the setup were rinsed and sterilized ultrasonically in 70% 2-propenol for 10 minutes, followed by deionized water for 10 minutes. Samples were then dried in a stream of nitrogen gas. The Gamry Echem Analyst software was used to fit the impedance data to the equivalent circuit and to calculate E_{corr} and i_{corr} from the potentiodynamic curves. White light interferometry scans were taken again after electrochemical tests to calculate average

surface roughness measurements and SEM was used as an additional characterization tool for the corroded surfaces in SE imaging mode.

3 - Results

3.1 – Metallurgy and Microstructural Characterization

Solution anneals generally resulted in dramatic grain coarsening of various degrees, dependent on carbon content, anneal time, and anneal temperature, for both LC and HC CoCrMo wrought alloys.
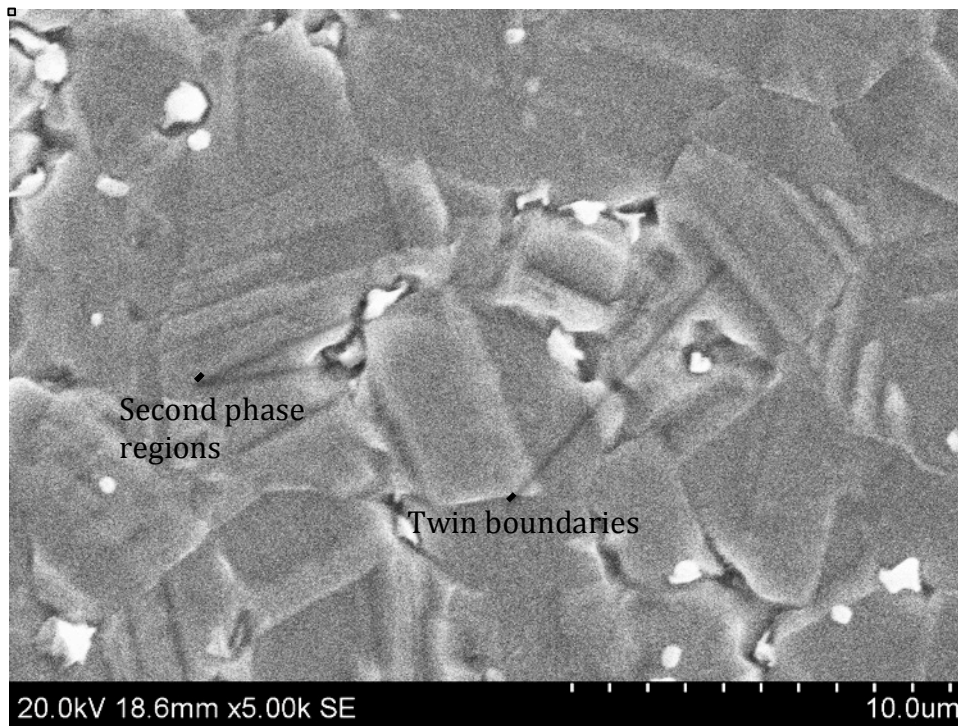
Figure 1. SEM micrograph of HC wrought CoCrMo alloy (no heat treatment); FCC matrix grains are ~ 4 μm in diameter while second phase (intermetallic and carbide [8]) regions are 0.5-1 μm in diameter.

For the HC wrought CoCrMo alloy, matrix grains were found to be on the order of 4 μm in diameter with smaller second phase regions precipitated mostly at the matrix grain boundaries, as seen in Figure 1. The matrix grains had numerous twin boundaries, known to be caused by stacking faults that arise during the hot working and cold working

processes used to get the material to the wrought state [8]. These stacking faults result in twinning more frequently when there is a lower stacking fault energy, leading to higher work hardening rates [13].

After a solution anneal at 1150°C for 2 hours, substantial grain coarsening occurred, which can be seen in Figure 2a. Stacking faults were still present even after the anneal was performed, and no significant second phase dissolution was observed. Figure 2b shows further grain coarsening in the HC CoCrMo samples after a 24-hour solution anneal at 1150°C. Again, stacking faults and twinning are still present (unlike grains of this size in as-cast CoCrMo alloys) in the grains, but partial carbide dissolution is observed.
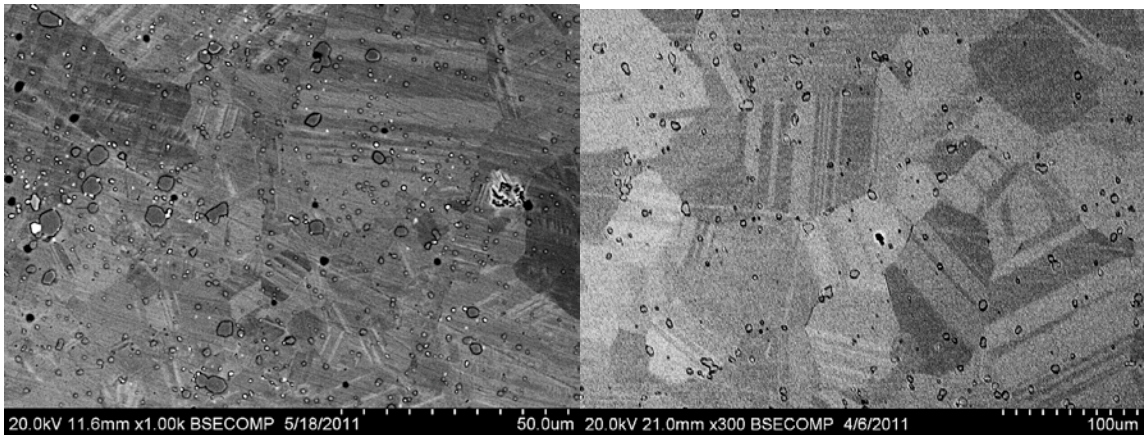
Figure 2. SEM micrographs of HC CoCrMo after (a) 1150°C/2h/water solution anneal (matrix grains ~ 20 μm in diameter, second phase regions ~ 1-3 μm in diameter) and (b) 1150°C/24h/water solution anneal (matrix grains ~ 150 μm in diameter, partially dissolved second phase regions ~ 1-3 μm in diameter).

An even more dramatic grain coarsening was observed in HC CoCrMo wrought alloy samples that were subject to 1230°C heat treatments (Figures 3a-b). Furthermore, partial second phase dissolution was observed as early as 2 hours into the 1230° solution anneal, as demonstrated in Figure 3a. However, even after 24 hours of solution anneal (inset of Figure 3b), there were still a few second phase regions remaining. This is in

7

accordance with Clemow & Daniell's findings, in which it took as long as 48 hours at a

solution anneal temperature to achieve complete carbide dissolution in some cases [9].
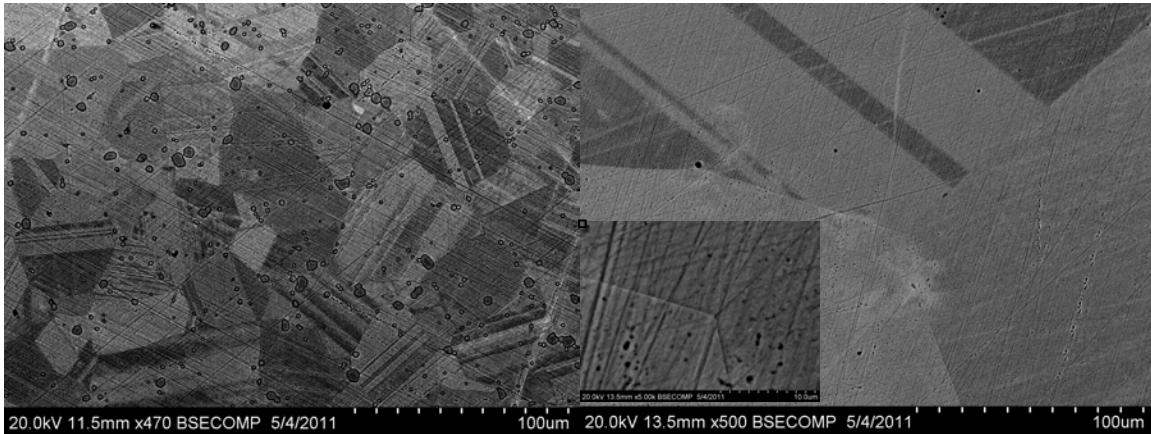
Figure 3. SEM micrographs of HC CoCrMo alloys after (a) 1230ºC/2h/water solution anneal (matrix grains ~ 55 μm in diameter, partially dissolved second phase regions ~ 3 μm in diameter), and (b) 1230ºC/24h/water solution anneal (matrix grains ~ 500 μm in diameter, inset: partially dissolved second phase regions ~ 0.5 μm in diameter).

For the LC CoCrMo wrought alloy, matrix grains were also found to be on the

order of about 4 μm with many stacking faults and twinned regions throughout, as

evidenced in Figure 4. However, no second phases were present, as is typical and

expected of low-carbon CoCrMo wrought alloys [11].
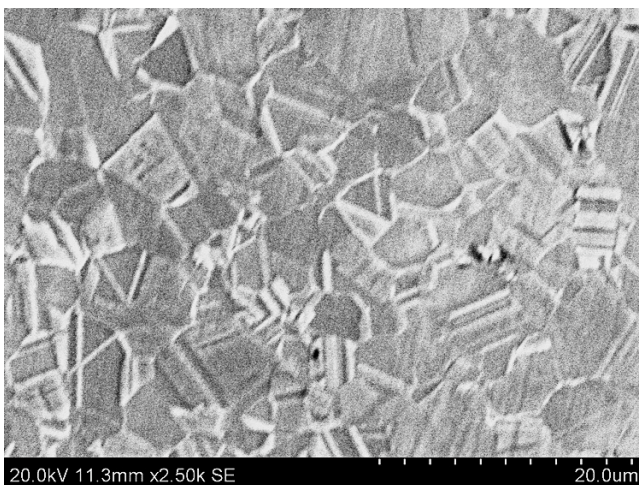
Figure 4. SEM micrograph of LC CoCrMo alloy (no heat treatment); matrix grains are ~ 4 μm.

The solution anneals of the low-carbon alloy (Figures 5-6) yielded more dramatic

grain coarsening than in the high-carbon alloy (Figures 2-3), due to the lack of second

phases affecting grain boundary mobility. As with the solution anneal effects on the wrought HC CoCrMo, grains coarsened more with longer anneal times and with the higher anneal temperature. A summary of the resulting grain sizes for all the heat treatments is given in Figure 7 and Table 3.
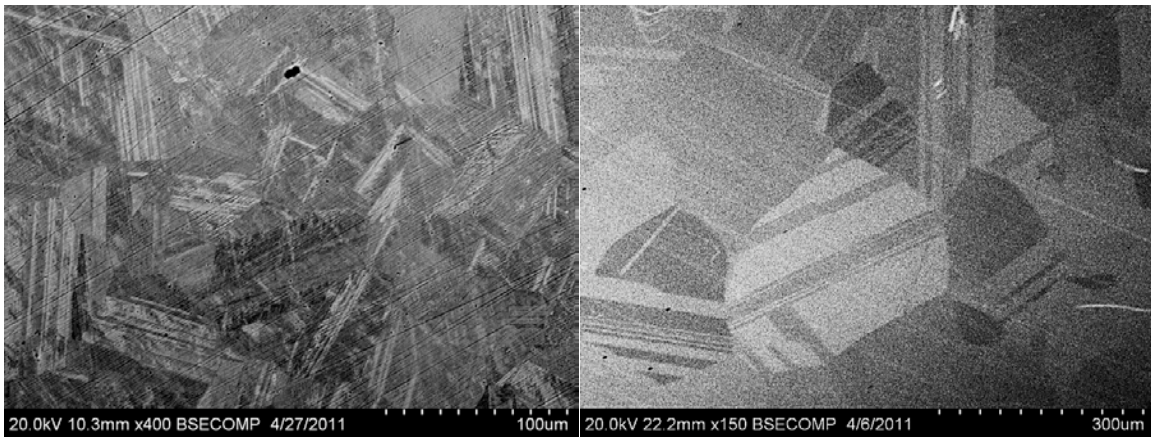
Figure 5. SEM micrographs of LC CoCrMo alloys after (a) 1150°C/2h/water solution anneal (grain size ~ 100 μm), and (b) 1150°C/24h/water solution anneal (grain size ~ 175 μm).
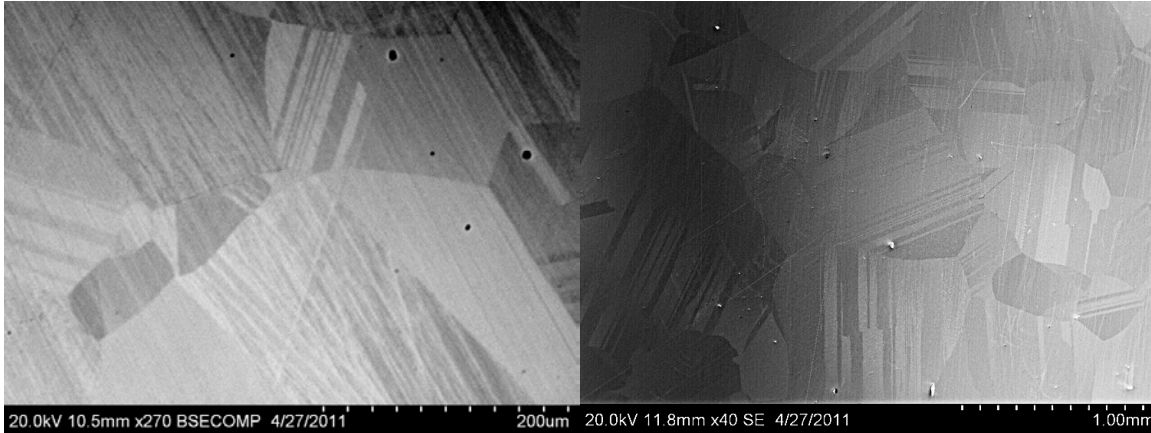
Figure 6. SEM micrographs of LC CoCrMo alloy after (a) 1230°C/2h/water solution anneal (grain size ~ 200 μm), and (b) 1230°C/24h/water solution anneal (grain size ~ 600 μm).

Table 3. FCC matrix grain size of solution annealed HC and LC wrought CoCrMo alloys

Heat Treatment	Low-Carbon	High-Carbon
No heat treatment	3 μm – 5 μm	3 μm – 5 μm
1150°C/2h/water	50 μm – 150 μm	10 μm - 40 μm
1150°C/24h/water	100 μm – 250 μm	50 μm – 200 μm
1230°C/2h/water	100 μm – 300 μm	30 μm – 80 μm
1230°C/24h/water	200 μm – 1000 μm	200 μm – 800 μm
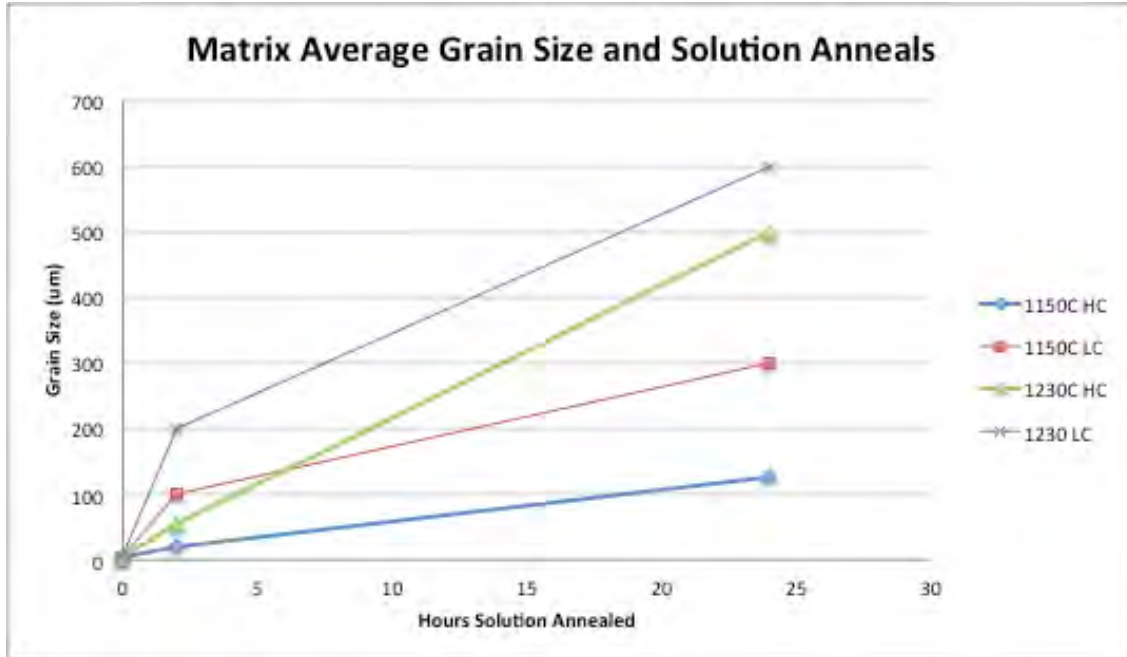
Figure 7. Summary of matrix grain coarsening in CoCrMo alloys over annealing time, by carbon content and anneal temperature.

3.2 – Electrochemical Tests

Data from open circuit potential tests, cyclic polarization (potentiodynamic) tests, and impedance spectroscopy were useful in assessing the corrosion behavior and passive film properties of the wrought and solution annealed CoCrMo alloys.

3.2.1 – Open Circuit Potentials

Open circuit potentials are one measure used to determine the potential at which the anodic and cathodic corrosion reactions cancel one another out. These values indicate a metal's tendency to corrode in the given electrolyte.

Figures 7a-c indicate that while there may not be a significant difference in E_{oc} between different heat treatments and different levels of alloy carbon content, the corroded samples exhibited a lower "tendency" to corrode than their uncorroded counterparts.
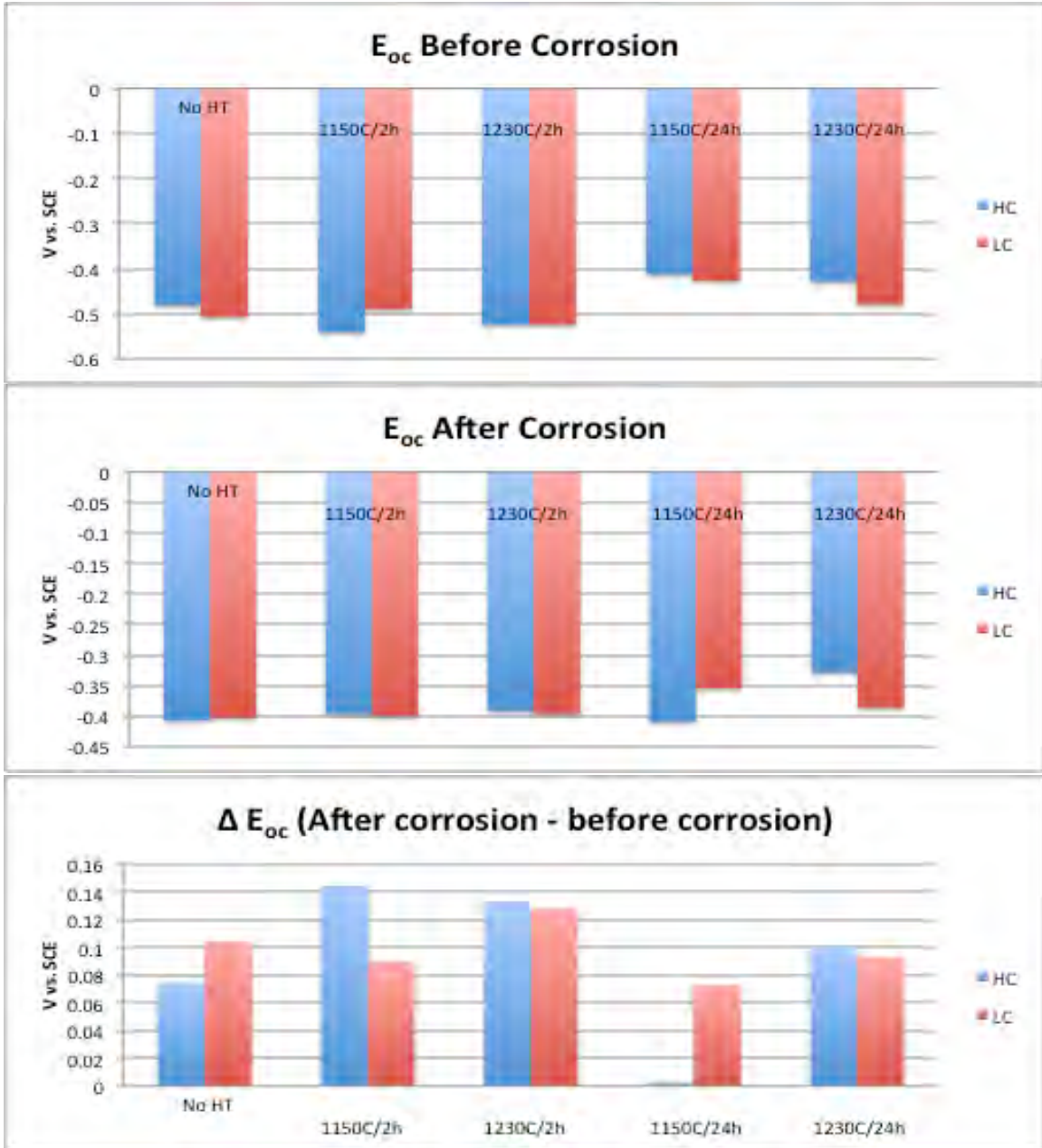
Figure 7a-c. Open circuit potentials of solution annealed HC and LC CoCrMo wrought alloys (a) before corrosion and (b) after corrosion. (c) E_{oc} had a positive difference after corrosion for each heat treatment.

3.2.2 – Impedance and Equivalent Circuit

Bode impedance plots were constructed to compare the passive film kinetics between samples, as seen in Figure 8. On the left side of the graph (lower frequencies), higher impedance values and a steeper slope would imply that the passive film is more

successful at limiting corrosion. However, the results show that there is no significant difference in passive film kinetics between experimental anneal conditions.
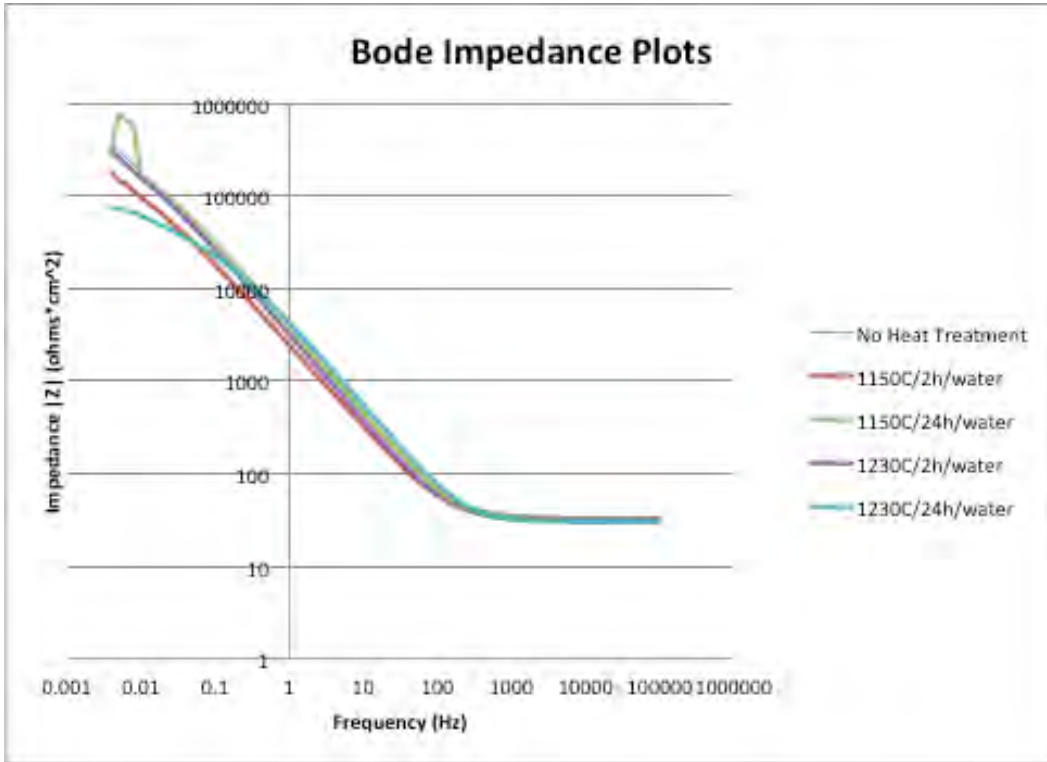
Figure 8. Bode impedance plot of solution annealed HC CoCrMo. The spike in impedance |Z| at 0.01 Hz for the 1150°C/24h/water solution anneal is experimental error which commonly occurs at very low frequencies and does not have any implications on the passive film strength.

In Figure 9, Bode phase plots were also used to compare the passive film strength. A broader range of frequencies with a high phase angle would imply a stronger passive film, so in this respect the 1230°C/24h/water solution anneal may have resulted in a weaker passive film.

Impedance vector data was broken down into the real and imaginary components, and Nyquist plots were created (Figure 10a-b) in an attempt to compare the corrosion resistance of the passive films. These plots are in the form of semicircle arcs, which would be complete and intercept the *Z'* axis again if the impedance were measured at low enough frequencies. Higher arcs result in higher *Z'* intercepts, which relate to the

polarization resistance, a quantity which indicates the material has better passive film

corrosion resistance. These plots indicate that the weaker (or lack of) solution anneals

may have a slightly stronger passive film in both the HC and LC CoCrMo wrought

alloys. This is consistent with the results seen in the Bode phase plots (Figure 9).
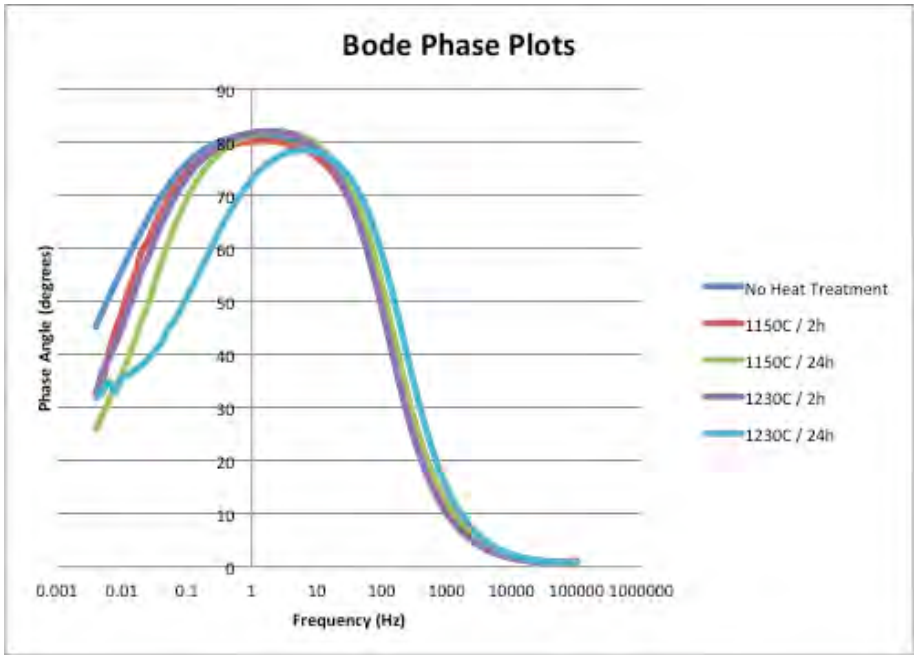
Figure 9. Bode phase plots of solution annealed HC CoCrMo. All solution anneals had similar phase angle properties with the exception of the 1230°C/24h/water experimental condition.
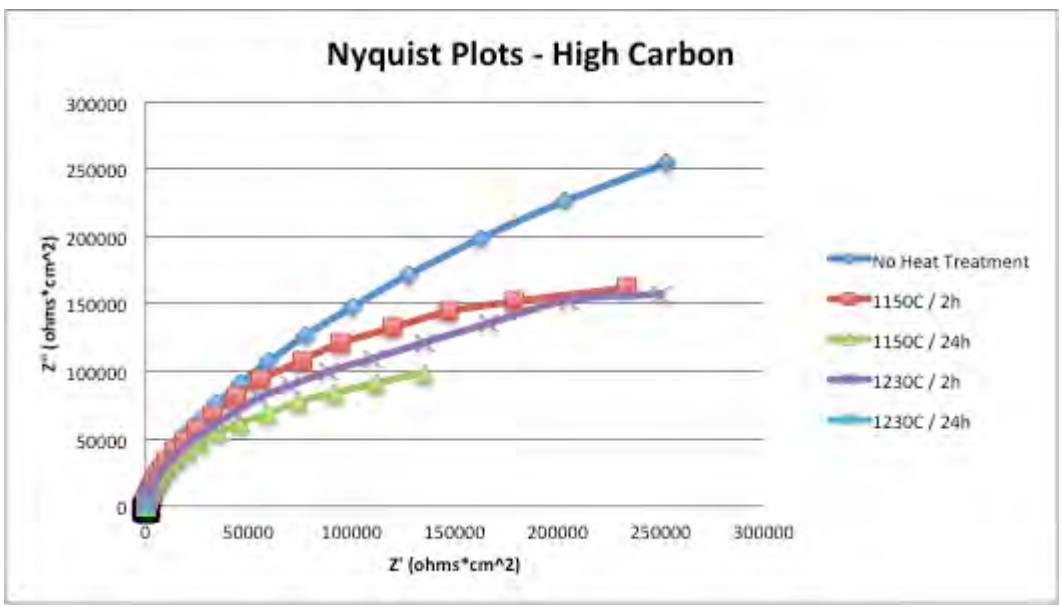
(a)
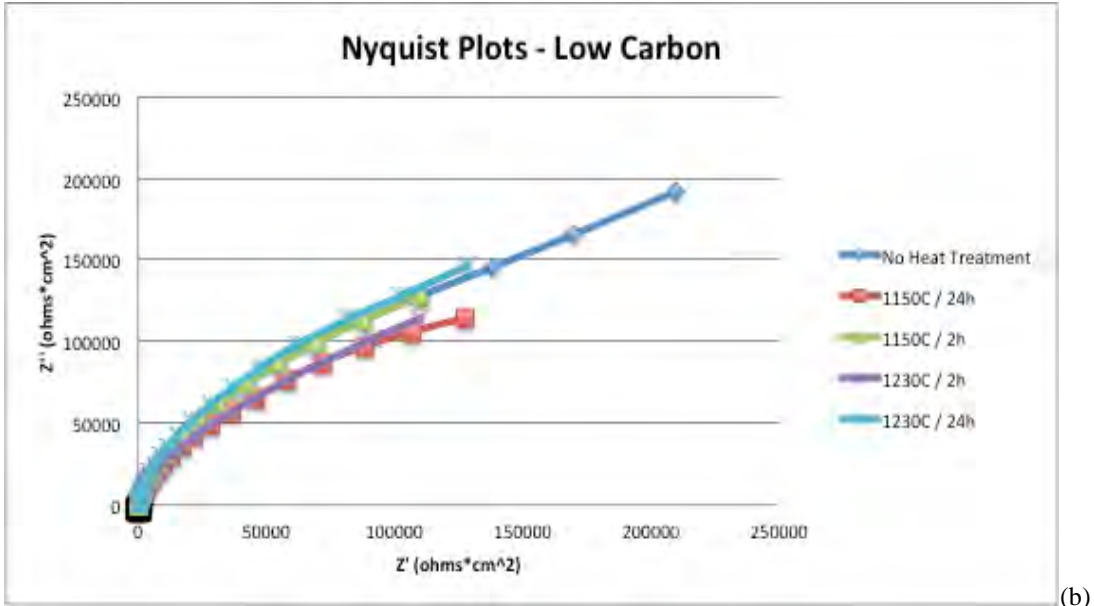
Figure 10. Nyquist plots of solution annealed (a) HC and (b) LC CoCrMo wrought alloy

Finally, the impedance data was fitted to a Randall's circuit. The solution resistance R_u values for all samples were very similar, as was expected since the electrochemical cell setups all used the same pH 7.4 buffered BCS. The polarization resistance R_p was also similar across all experimental conditions as seen in Figure 11, indicating the differences seen in the Bode phase plots and Nyquist plots may not be statistically significant.
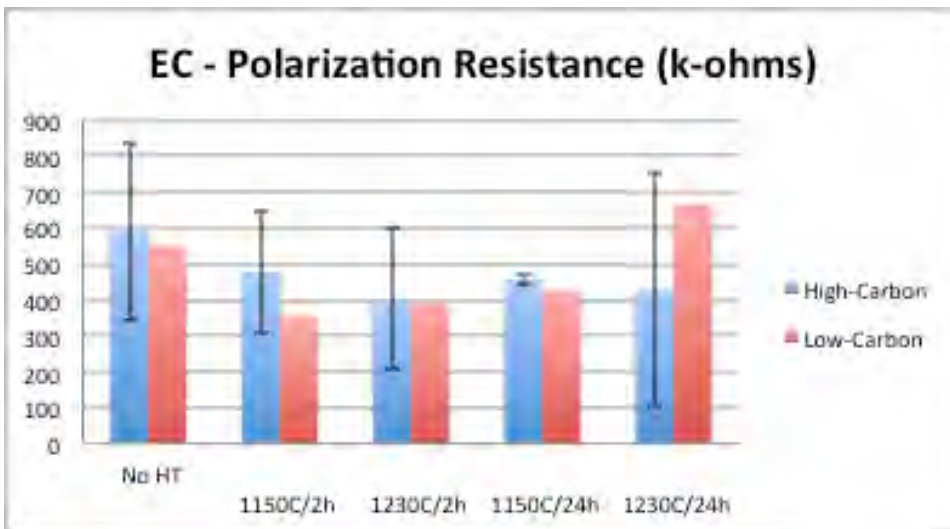
Figure 11. Polarization resistance R_p of fitted equivalent Randall's circuit for solution annealed HC and LC CoCrMo wrought alloys.
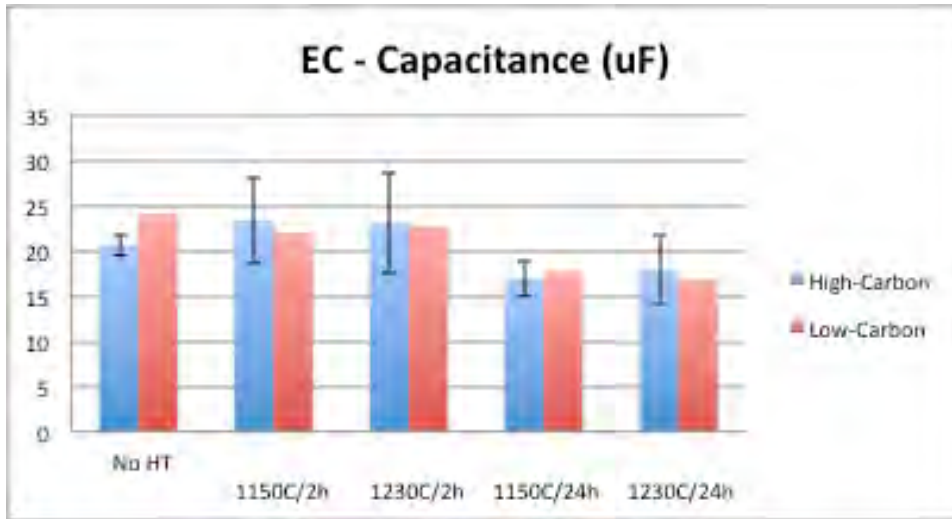
Figure 12. Capacitance C_f of fitted equivalent Randall's circuit for solution annealed HC and LC CoCrMo wrought alloys.

The equivalent circuit's capacitance C_f also did not show any statistically significant variation across experimental anneal conditions, as seen in Figure 12. However, there may be a trend for lower C_f values for the 24-hour solution anneals. In an electrical circuit, a lower capacitance refers to less charge accumulating on the plates of the capacitor. Similarly, in the electrochemical setup, a lower equivalent capacitance refers to less total charge (metal cation and electron) transfer across the CoCrMo-BCS interface, and thus, less corrosion.

3.2.3 Potentiodynamic (Cyclic Polarization)

An applied DC potential was applied from -0.8V to 1.8V to corrode the samples, and the resulting current was measured. Current density was calculated from this, taking the exposed sample area of the working electrode to be 0.38465 cm^2. Potentiodynamic curves were constructed in Figures 13-14.

These curves indicate that for all solution anneals (as well as in the absence of heat treatments), the HC CoCrMo alloys (Figure 13) have the same passive zone from about -0.25V to 0.5V, again indicating that their passive film kinetics do not vary with

15

length or temperature of solution anneal. Figure 14 shows a similar response for most solution annealed LC CoCrMo alloys, with the exception of the 24-hour 1150°C heat treatment. This is assumed to be experimental error, as it does not follow the typical corrosion behavior of any CoCrMo alloy, and is attributed to proteins from the BCS adsorbing onto the sample's surface during the cyclic polarization test.
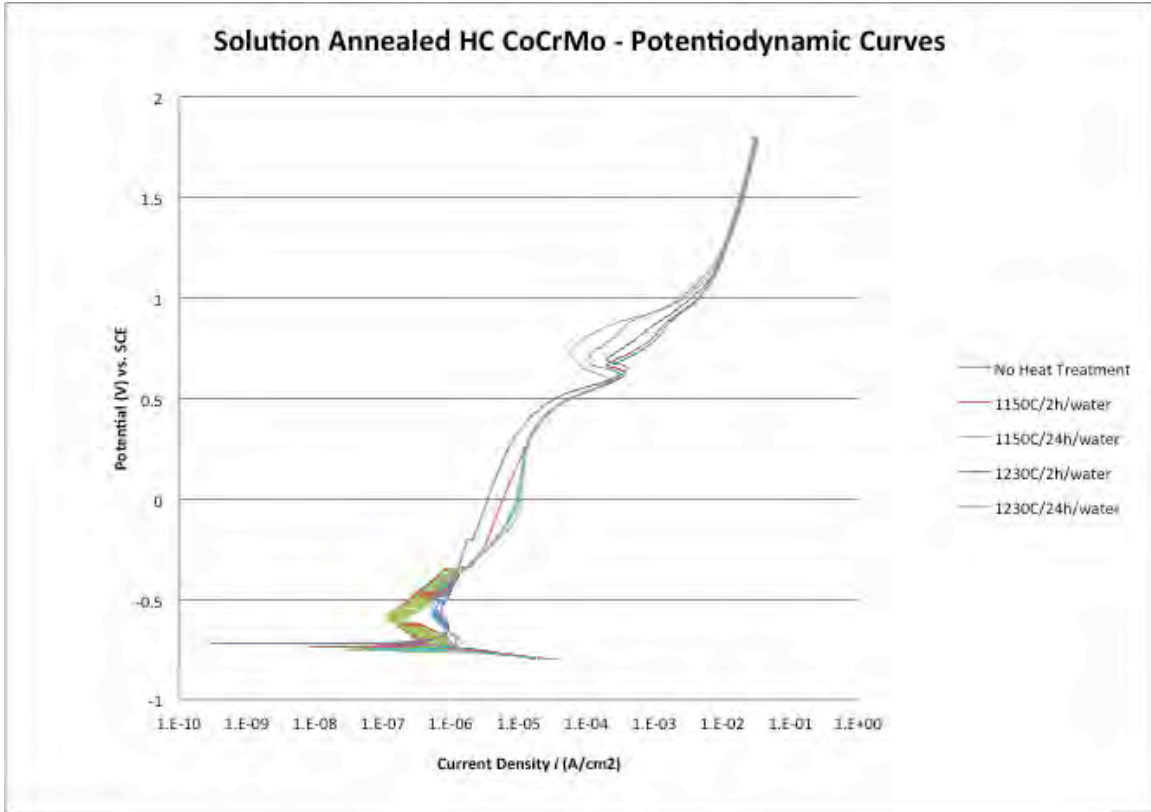
Figure 13. Potentiodynamic curves for solution annealed HC CoCrMo wrought alloys.

The main dip in current density in the potentiodynamic curves is also analyzed for the important corrosion parameters E_{corr} and i_{corr}. The approximated corrosion potential E_{corr} values for each experimental anneal condition are summarized in Figure 15. These values show no statistically significant difference across heat treatments, as is commonly the case in cyclic polarization tests on CoCrMo biomedical alloys. However, for the

shorter solution anneals, the low-carbon samples all had lower E_{corr} values, indicating that

they may have had a higher tendency to corrode.
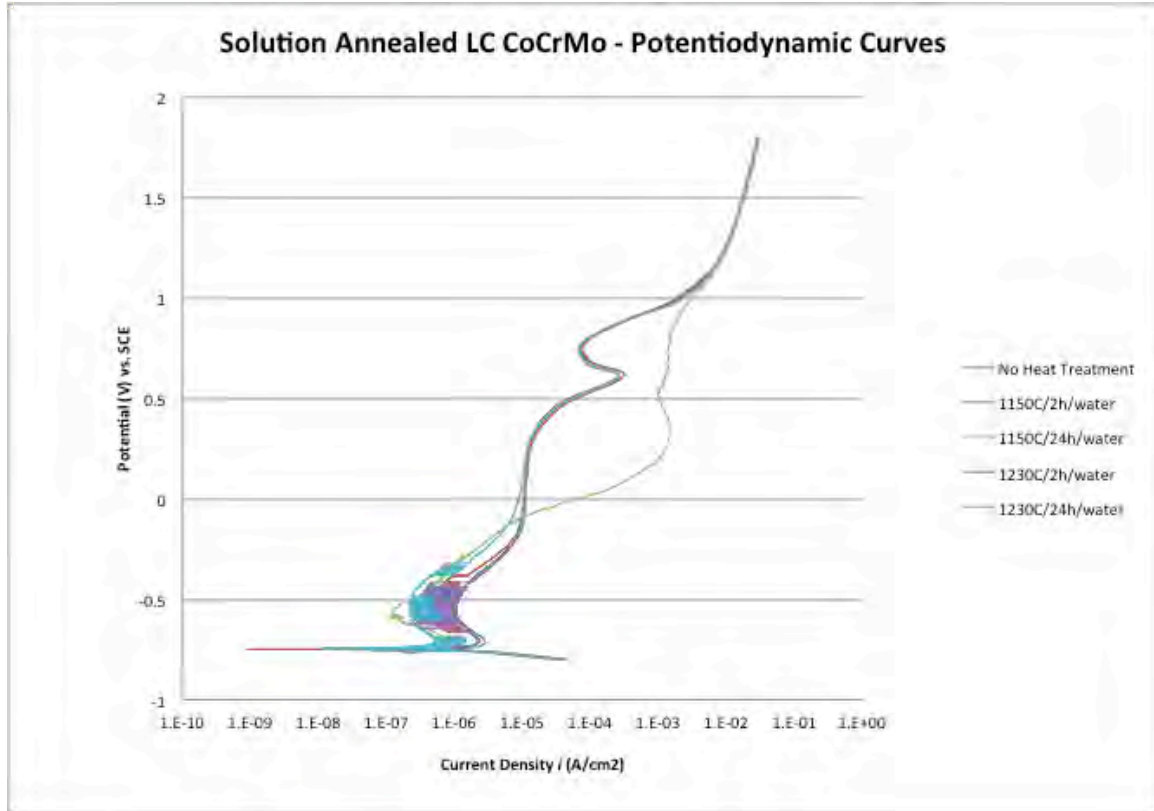
Figure 14. Potentiodynamic curves for solution annealed LC CoCrMo wrought alloys.
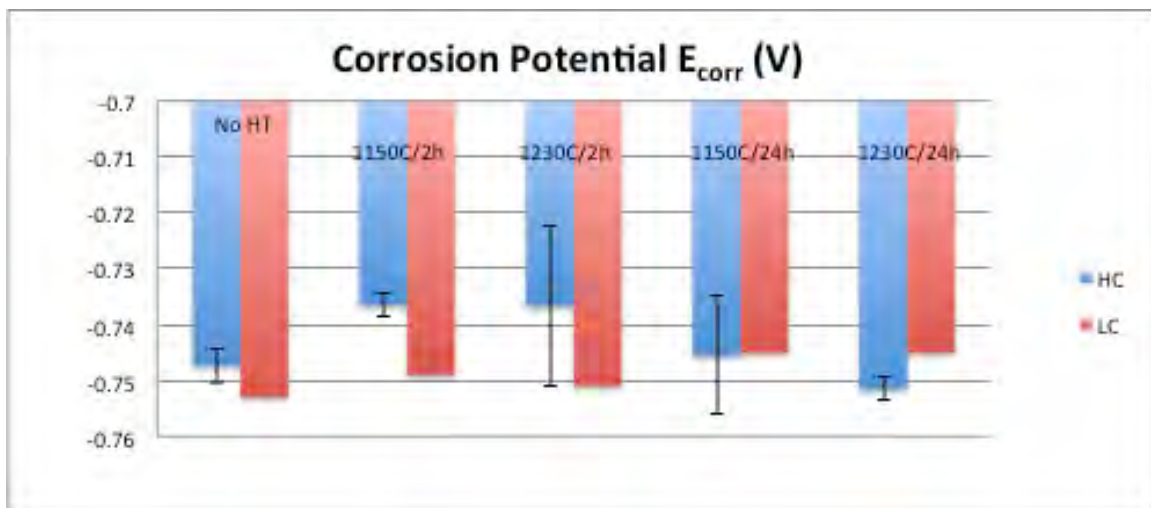
Figure 15. Corrosion potential E_{corr} for solution annealed CoCrMo wrought alloys

Current density i_{corr} was a more useful parameter in comparing corrosion

properties among the experimental conditions, demonstrated in Figure 16. All solution

anneals resulted in a dramatically lower current density, indicating a lower rate of

corrosion. This data also confirms previous findings on the generally higher corrosion

rates of LC CoCrMo alloys [14].
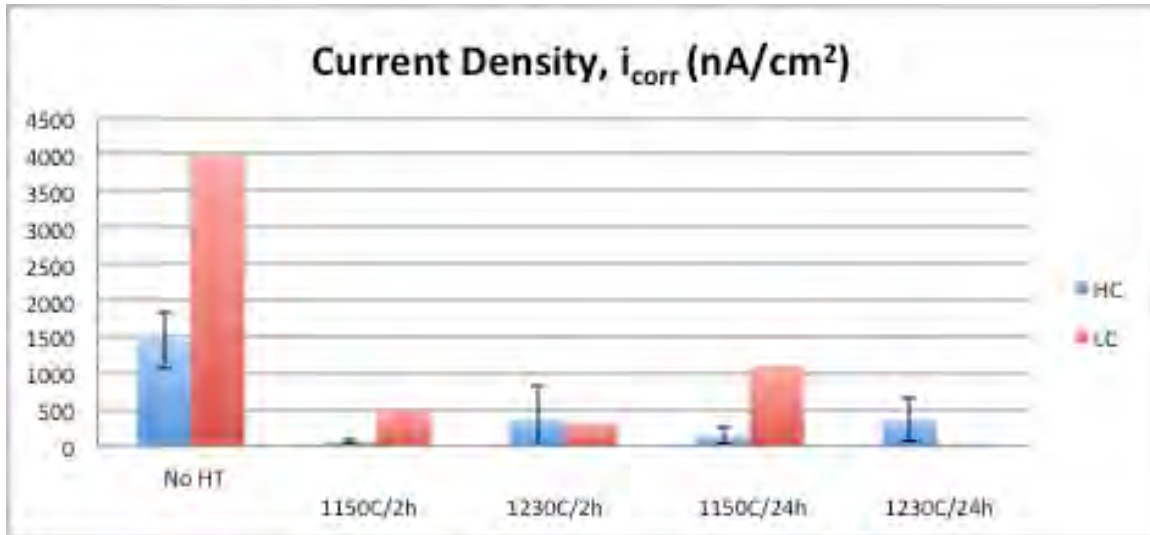
Figure 16. Current density i_{corr} at corrosion potential for solution annealed CoCrMo wrought alloys

3.3 White Light Interferometry and SEM After Corrosion

Topographic maps (Figures 17a-b) of the non-solution annealed HC CoCrMo

alloy did not reveal any details about any selective corrosion behavior, but only that the

surface was very rough after corrosion. These white light interferometry images are

unable to provide much details since this method has a limit on lateral resolution [15].

SEM micrographs revealed in Figure 17c that the corroded region consists of numerous

spherical corrosion pits on the order of 1-3 μm in diameter. Since these corrosion pits are

larger than the second phases and almost as large as the grains themselves, it is not

possible to directly tell from these results if corrosion has any preferential behavior in HC

CoCrMo wrought alloys in the absence of solution annealing. Additionally, it seems the second phases were removed from the surface during corrosion.
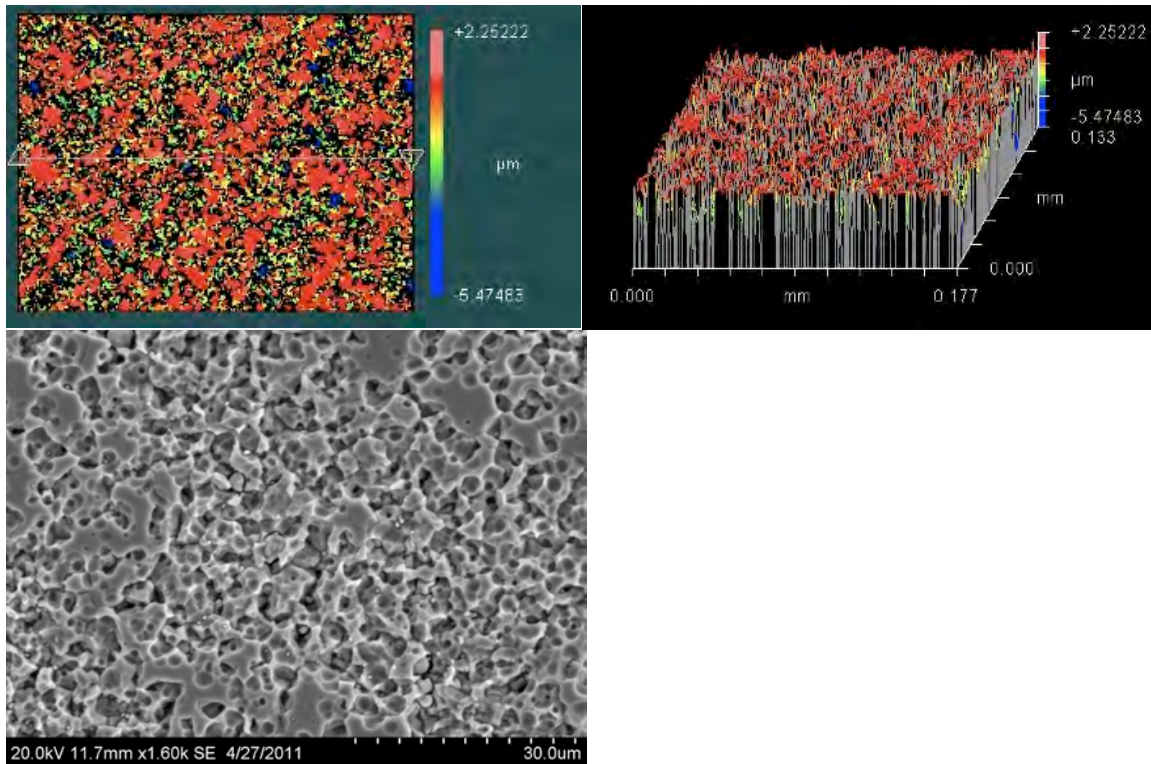
Figure 17. Corroded HC CoCrMo wrought alloy without solution anneal: white light interferometry (a) topographic view and (b) perspective view, and (c) SEM micrograph of surface.

The 1150°C/2h/water solution annealed HC CoCrMo wrought alloy's interferometry images (Figure 18a-b) after corrosion demonstrated that this surface is less rough than the corroded alloy without any solution annealing (Figure 17a-b). However, the grains again are too fine, even at an average of ~20 μm, to show any direct evidence of corrosion targeting any grain boundaries. SEM imaging of this corroded sample reveals in Figure 18c that these corrosion pits are the same spherical dips 1-3 μm in size. These micrographs also reveal that the (now enlarged) second phase regions are still present after corrosion, but these phases appear to be surrounded by corrosion pits. It is likely that corrosion does target phase boundaries, and not the second phases themselves.

This is in contrast to Montero-Ocampo *et al.*'s conclusions that corrosion targeted the second phases themselves [16].
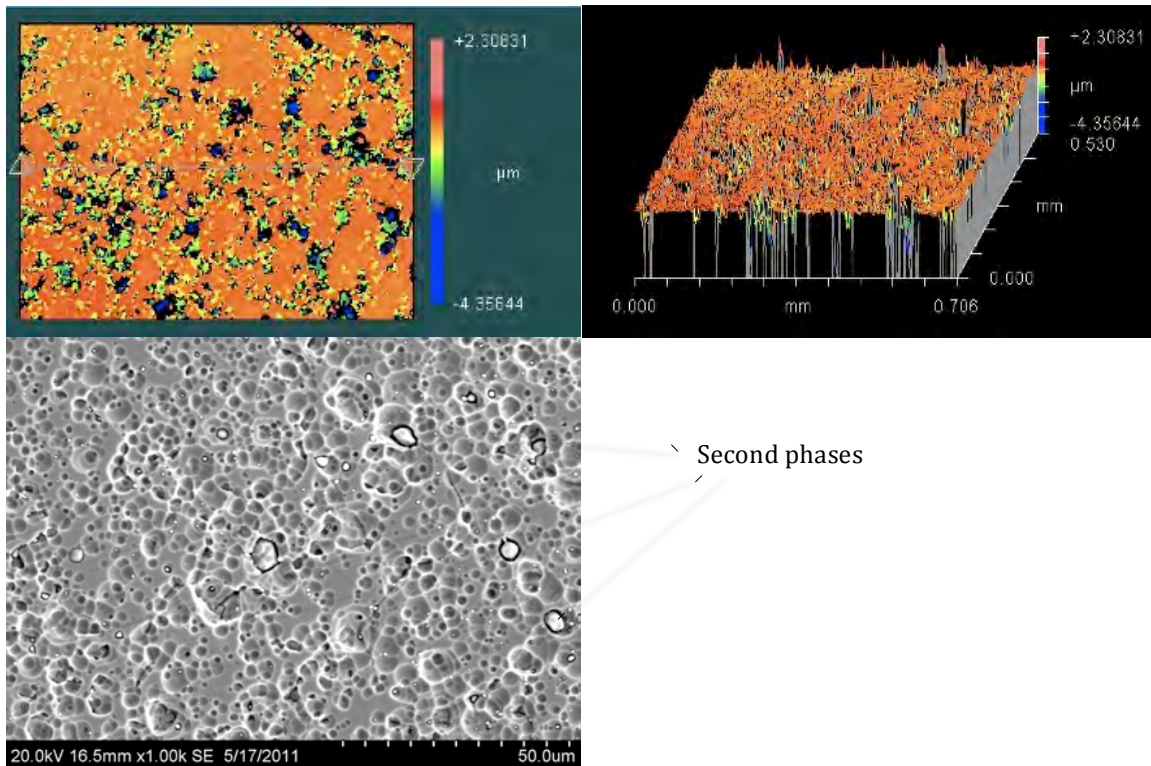
Figure 18. Corroded HC CoCrMo wrought alloy after 1150°C/2h/water solution anneal: white light interferometry (a) topographic view and (b) perspective view, and (c) SEM micrograph of surface.

Specifics of corrosion behavior were seen more easily in the 1150°C/24h/water solution annealed HC CoCrMo alloy. The grains in this experimental condition were large enough to be seen readily in an optical microscope, and white light interferometry scans in Figures 19a-b show that there are both spherical corrosion pits within matrix grains and preferential corrosion at some grain boundaries. Furthermore, SEM images of the corroded surface (Figure 19c) demonstrate that some grain boundaries are corroded very heavily and others not at all. Preferential grain boundary corrosion in HC CoCrMo alloys has been documented previously [16], but there was no mention of some grain boundaries corroding more than others. It is probable that the corrosion pits not at the grain boundaries are at the phase boundaries of the second phase precipitates.
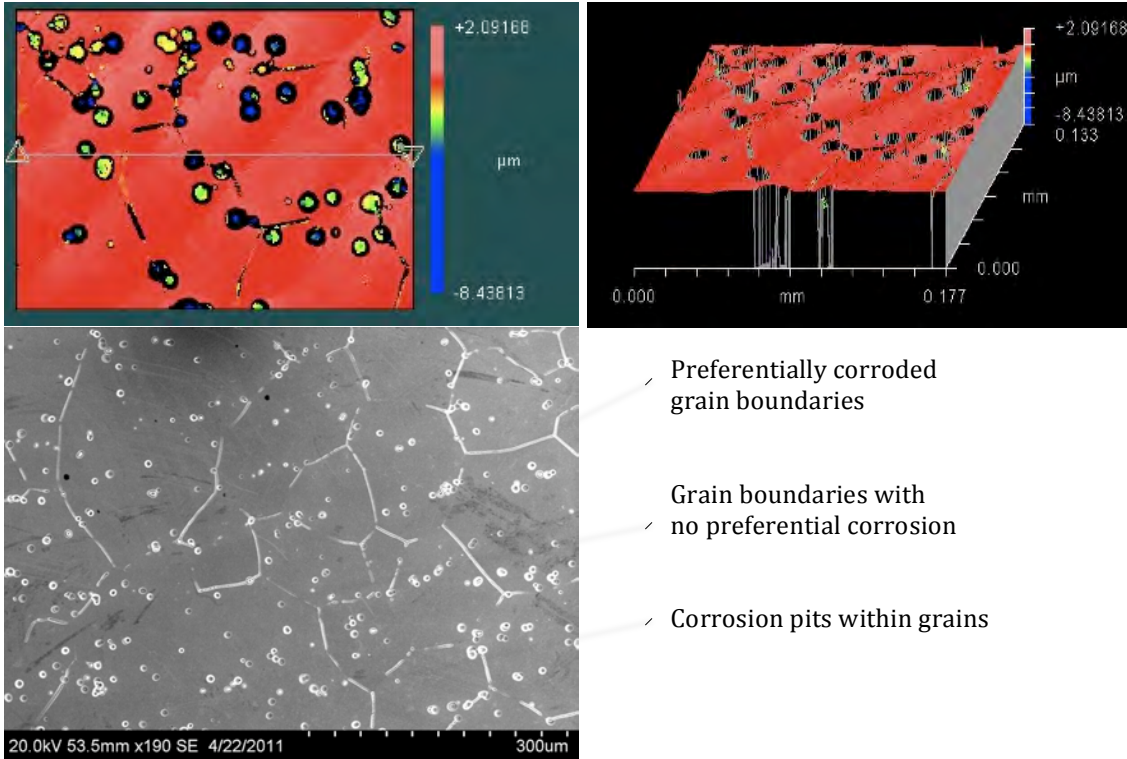
Figure 19. Corroded HC CoCrMo wrought alloy after 1150°C/24h/water solution anneal: white light interferometry (a) topographic view and (b) perspective view, and (c) SEM micrograph of surface.

Similar corrosion behavior was seen in the corroded surfaces of the 1230°C/2h/water solution annealed HC CoCrMo, shown in Figures 20a-c. Corrosion specifically attacked some of the grain boundaries, as well as phase boundaries at the second phases which resulted in corrosion pits within the matrix grains. More spherical corrosion pits are seen near the grain boundaries in this solution anneal condition, which corresponds to the lower degree of second phase dissolution for the 1230°C/2h/water heat treatment (Figure 3a) than for the 1150°C/24h/water heat treatment (Figure 2b).

Samples annealed at 1230°C/24h/water corroded in a similar manner with some grain boundaries selectively attacked (as seen in Figure 21c). Fewer corrosion pits were present than for HC samples with any other solution anneal conditions (Figures 21a-c), most likely due to the partial carbide and intermetallic dissolution seen after this heat treatment.
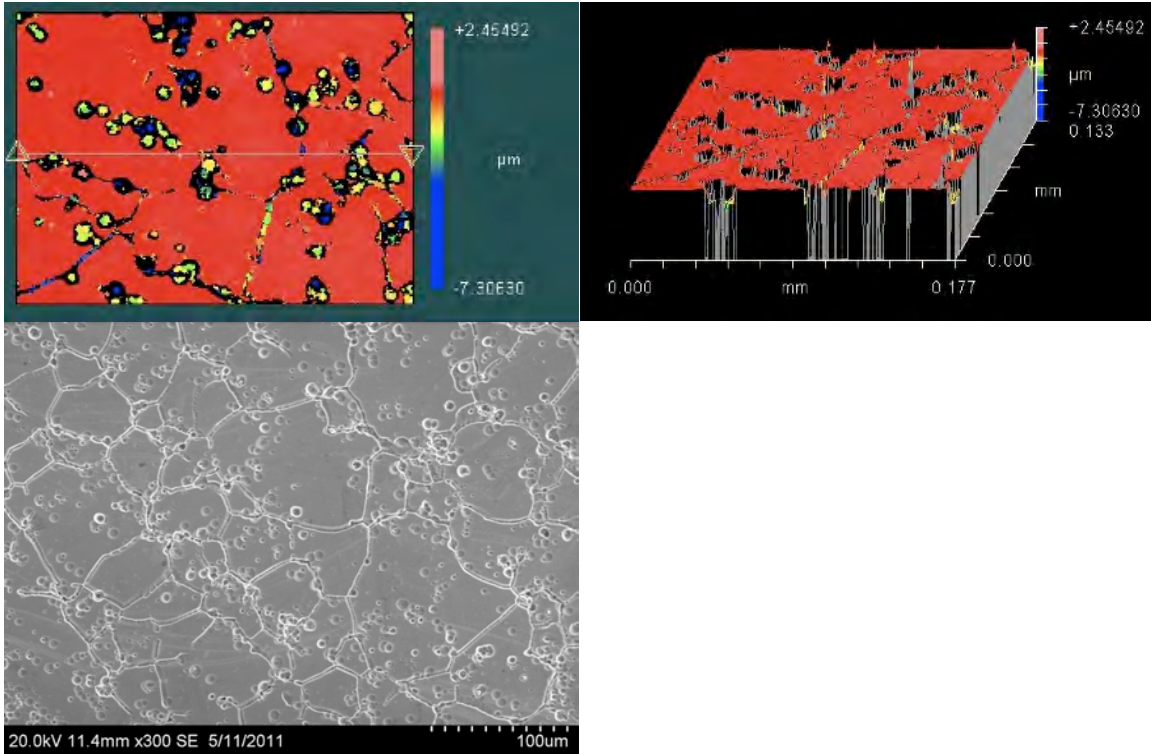
Figure 20. Corroded HC CoCrMo wrought alloy after 1230°C/2h/water solution anneal: white light interferometry (a) topographic view and (b) perspective view, and (c) SEM micrograph of surface.
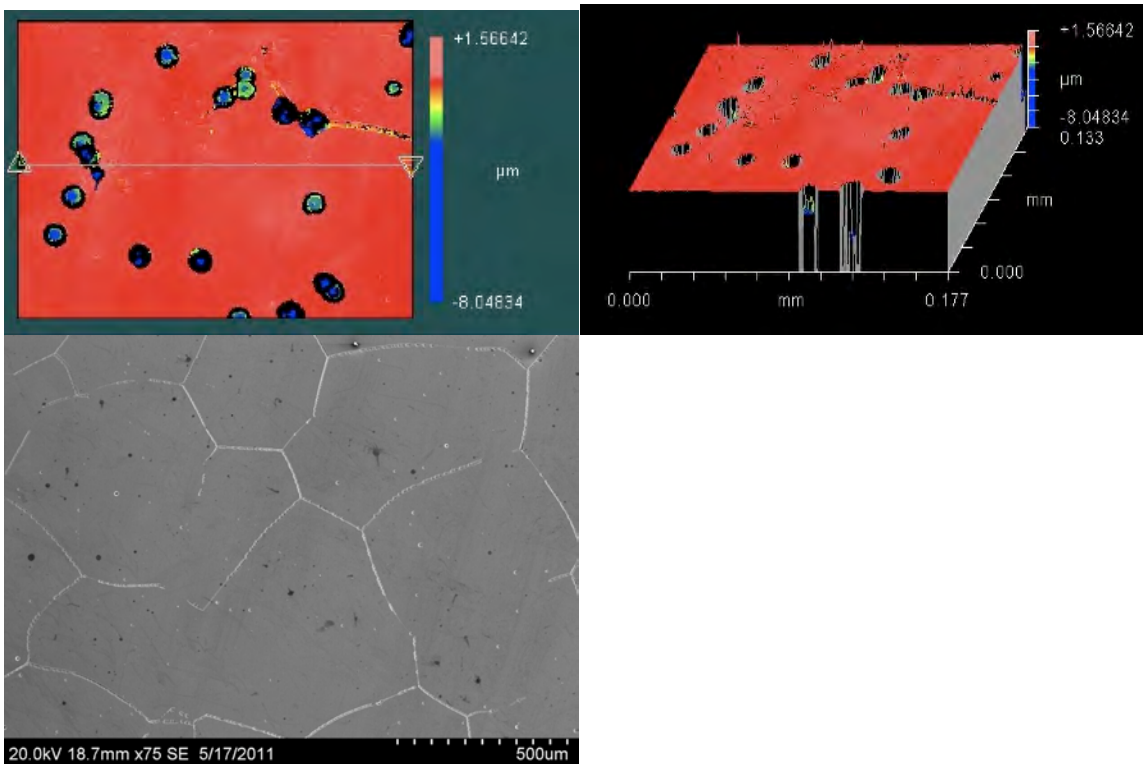
Figure 21. Corroded HC CoCrMo wrought alloy after 1230°C/24h/water solution anneal: white light interferometry (a) topographic view and (b) perspective view, and (c) SEM micrograph of surface.

All low-carbon CoCrMo samples corroded very differently from their high-carbon counterparts. The LC CoCrMo wrought alloy without any solution annealing did not exhibit any preferential corroding, as seen in Figures 22a-c. There were a few corrosion pits present, but far less than for the non-solution annealed HC CoCrMo (Figure 17c), and these are attributed to the proteins in the BCS bringing about occasional corrosion pits on the surface. Any variations in topography seen in Figures 22a-b were very minor (a few hundred nanometers) compared to topographic variations seen in the HC samples at phase boundaries and select grain boundaries, and did not seem to correlate with any microstructural features on the LC wrought CoCrMo such as grain boundaries.
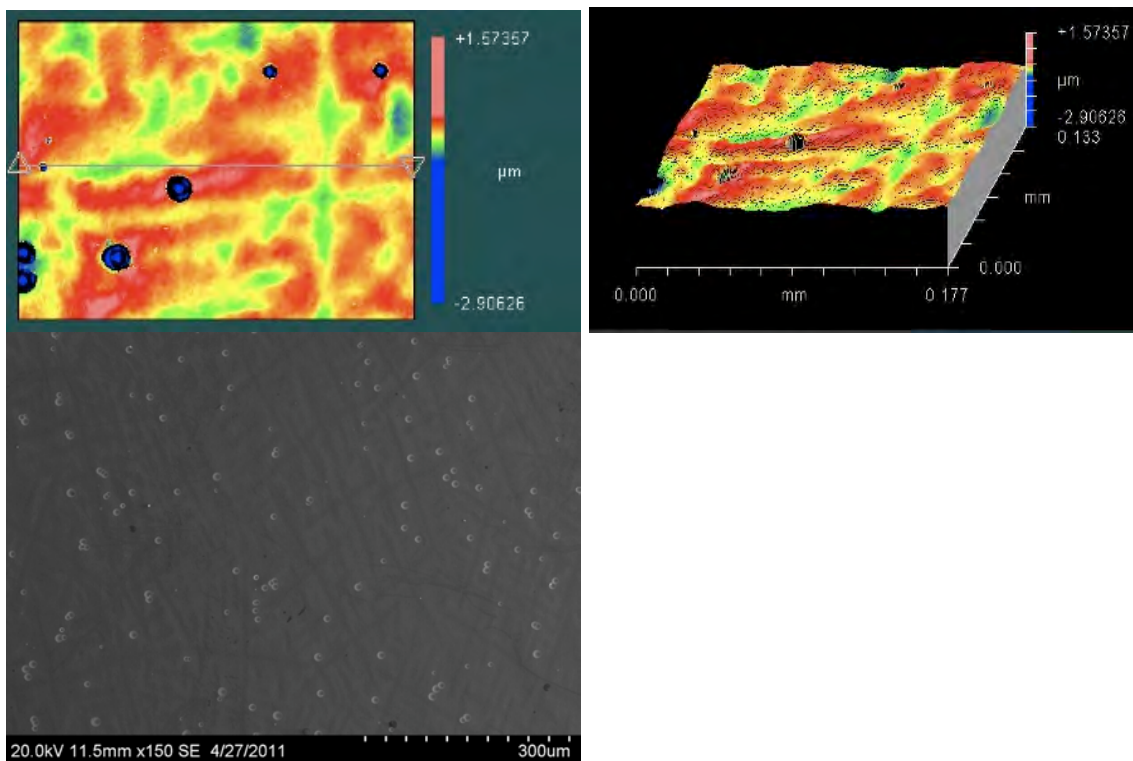
Figure 22. Corroded LC CoCrMo wrought alloy without solution anneal: white light interferometry (a) topographic view and (b) perspective view, and (c) SEM micrograph of surface.

When the LC CoCrMo samples were solution annealed at 1150°C for two hours, the corrosion behavior was similar to the non-solution annealed low-carbon alloy.

However, in this case, it can be seen that the slight differences in topography (Figures 23a-b) were at the twin boundaries in the grains, as seen in Figure 23c. There was no preferential corrosion at grain boundaries or at the twin boundaries themselves, but this indicates that electrochemical corrosion may affect certain orientations of grains in different ways. Again, these differences in topography were on the order of a few hundred nanometers.
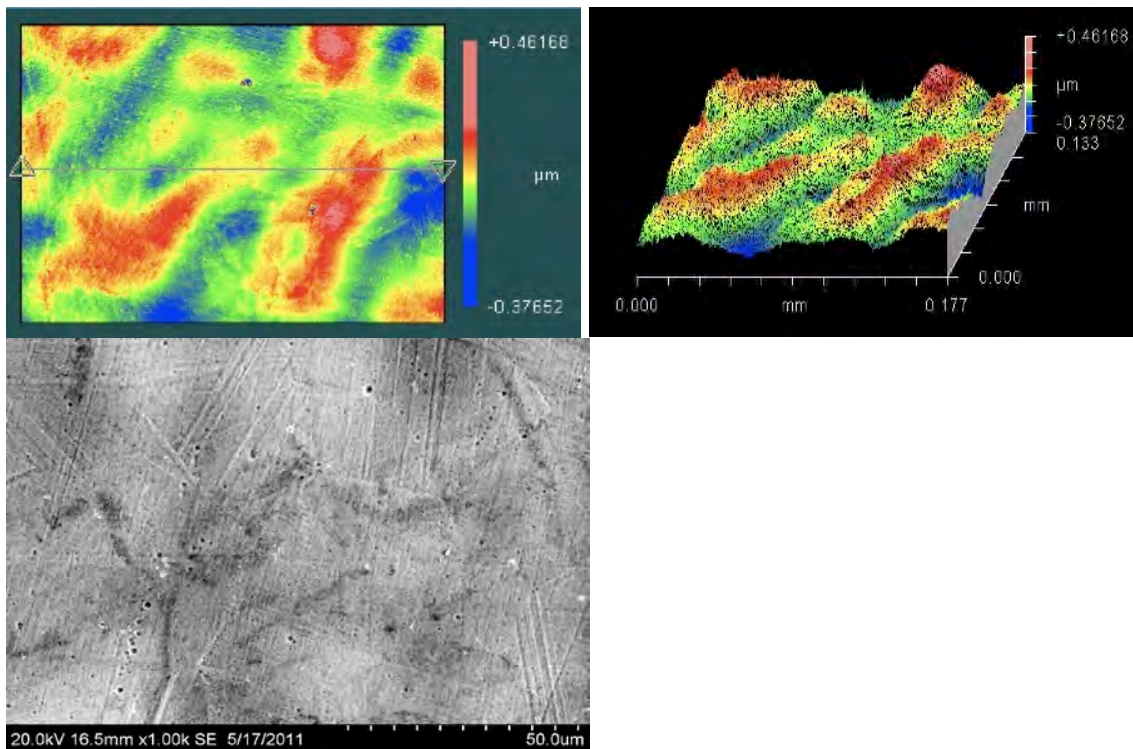
Figure 23. Corroded LC CoCrMo wrought alloy after 1150°C/2h/water solution anneal: white light interferometry (a) topographic view and (b) perspective view, and (c) SEM micrograph of surface.

A 24-hour solution anneal at this same temperature (1150°C) yielded similar behavior for the LC CoCrMo wrought alloy with no preferential corrosion at grain boundaries, but slightly more corroded areas at certain grain orientations, as seen by the visible twinning in Figures 24a-b. Other features visible on the surface (Figure 24c) were attributed to the effect from proteins in the BCS. The 1230°C/2h/water solution annealed LC CoCrMo alloy corroded in the same manner (Figures 25a-c).
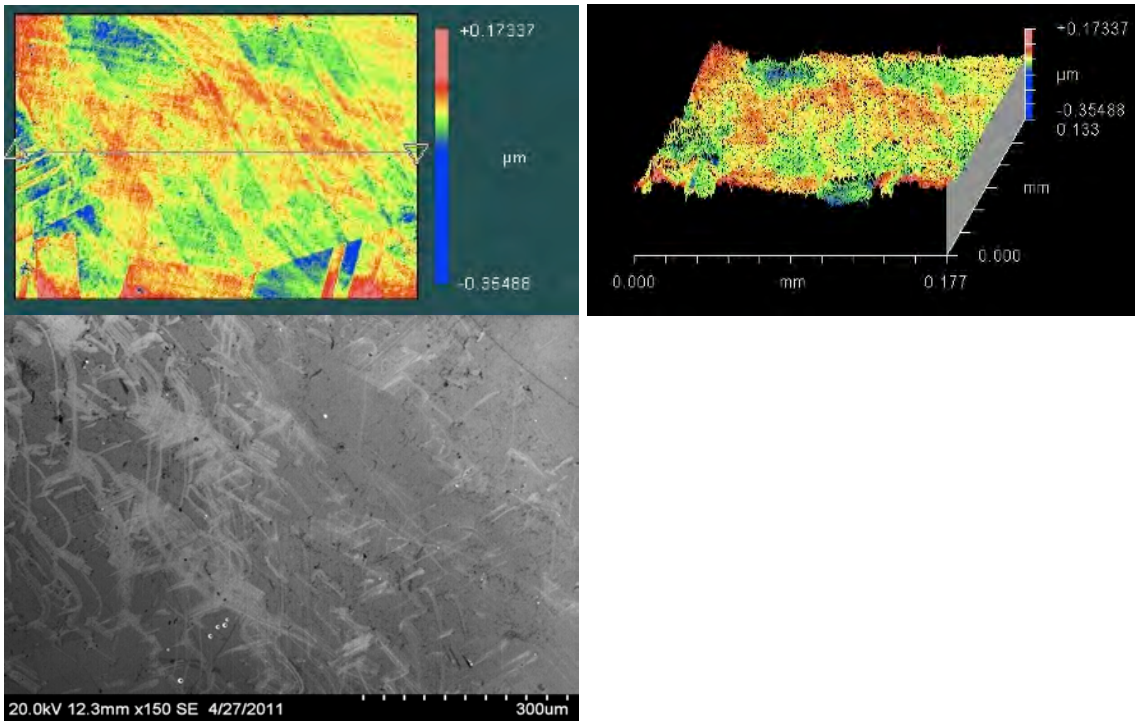
Figure 24. Corroded LC CoCrMo wrought alloy after 1150°C/24h/water solution anneal: white light interferometry (a) topographic view and (b) perspective view, and (c) SEM micrograph of surface.
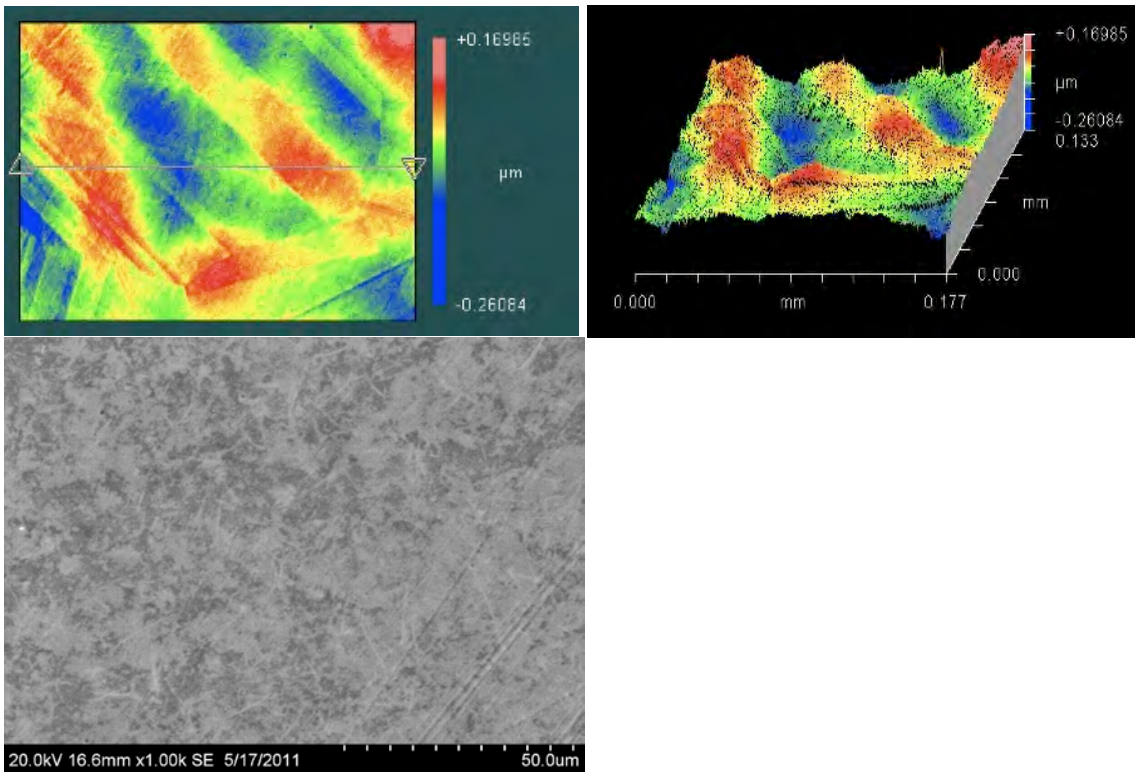
Figure 25. Corroded LC CoCrMo wrought alloy after 1230°C/2h/water solution anneal: white light interferometry (a) topographic view and (b) perspective view, and (c) SEM micrograph of surface.

Finally, the 1230°C/24h/water heat treated low-carbon CoCrMo exhibited some pitting after corrosion (Figures 26a-c), which was most likely caused by the proteins present in the electrolyte. Again, a slight topographic variation was seen across twin boundaries, presenting evidence that grain orientation may influence the amount of corrosion occurring at a given region.
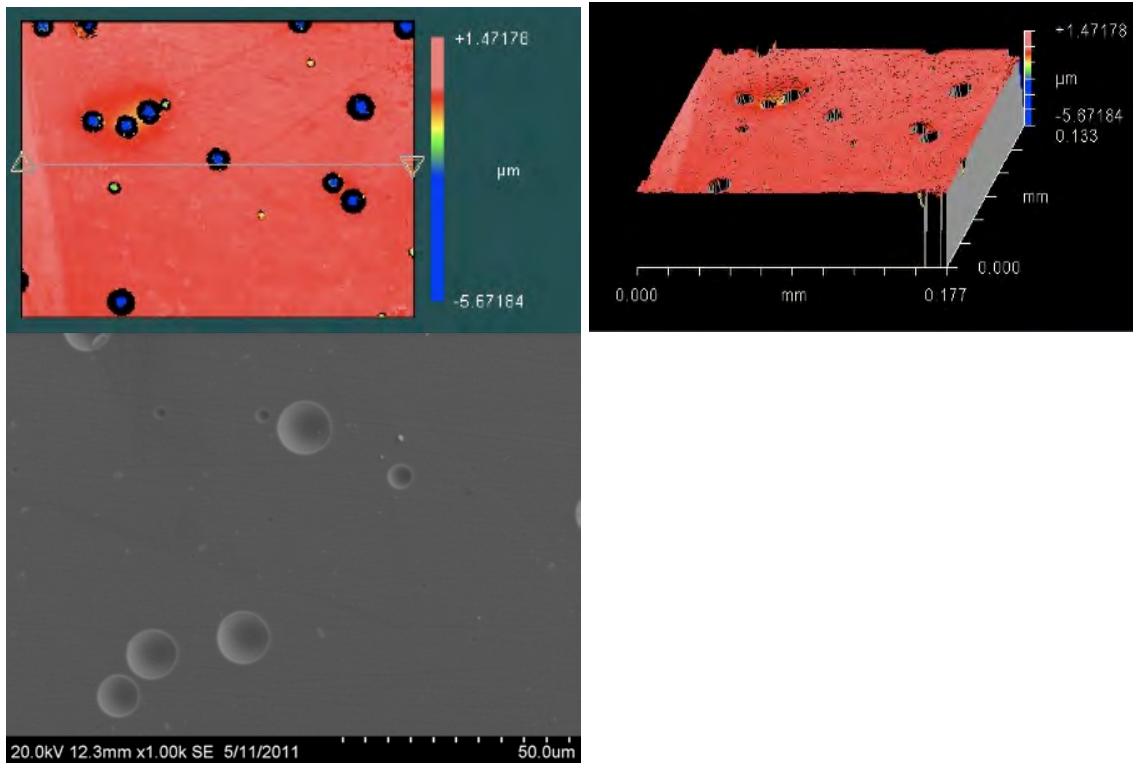
Figure 26. Corroded LC CoCrMo wrought alloy after 1230°C/24h/water solution anneal: white light interferometry (a) topographic view and (b) perspective view, and (c) SEM micrograph of surface.

The surface roughness seen in the white light interferometry scans was quantified and plotted against solution anneal time as seen in Figure 27. For the LC CoCrMo alloy (green triangles and purple crosses), the roughness caused by corrosion decreased slightly with increased anneal time and higher solution anneal temperature. The HC CoCrMo alloy (blue diamonds and red squares) had similar effects, but higher roughnesses at each point.
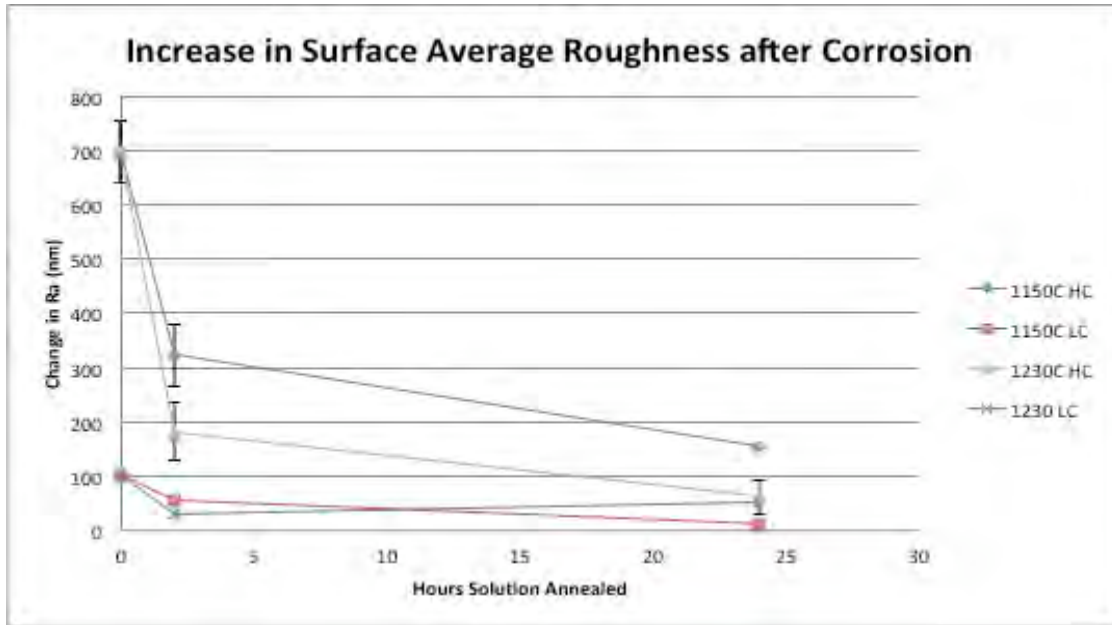
Figure 27. Surface average roughness from corrosion

4 - Discussion

4.1 – Corrosion Resistance and Passive Film Behavior

Open circuit potential tests and extrapolated values of the corrosion potential E_{corr} demonstrated that carbon content and the solution annealing did not affect the tendency of the CoCrMo alloys to corrode. This is, in part, due to the success of the passive film in remaining an effective kinetic barrier both in the absence and presence of various solution anneals.

There is, however, a significant decrease in the corrosion rate seen in the solution annealed alloys. Additionally, even though solution annealing results in various degree of second phase dissolution, the high-carbon CoCrMo wrought alloy still exhibits better corrosion resistance than its low-carbon counterparts, indicating that the dissolved carbon in the γCo matrix still plays a crucial part in the superiority of the HC alloy.

4.2 - Preferential Corrosion

The high-carbon alloys exhibited preferential corrosion at phase boundaries and at matrix grain boundaries. This may explain the reduced corrosion rates for solution annealed HC CoCrMo, since once the corrosion pits begin to form, the surface is unpassivated, removing the main kinetic barrier for corrosion. Montero-Ocampo *et al*. also observed preferential grain boundary corrosion in HC cast CoCrMo alloy, but did not observe any grain boundaries which were not preferentially corroded [16]. This study highlights the phase boundary corrosion seen next to the carbide and intermetallic phases, as well as the lack of targeted corrosion at certain grain boundaries.

Multiple authors reported Cr-segregation at phase and grain boundaries of CoCrMo alloys [17, 18], and this chromium depletion may explain the preferential corrosion seen at the phase boundaries. However, this is not the main mechanism explaining the preferential corrosion at the grain boundaries of the HC CoCrMo. Chromium depletion at grain boundaries has been observed in both high-carbon and low-carbon CoCrMo [18], and preferential grain boundary corrosion was only seen in the high-carbon alloys. Additionally, all grain boundaries exhibit chromium segregation, and not all grain boundaries experienced preferential corrosion.

Therefore, it is more likely that grain boundary corrosion depends on the relative orientations of the adjacent grains. The mild variation in corrosive attack seen in the low-carbon alloys at twinned regions suggests that corrosion is sensitive to the crystallographic orientation. Grain boundaries themselves are a separate phase and are essentially a distorted section of the lattice, a few unit cells across as seen in Figure 28. In other metallic materials, preferential inter-grain corrosion was also observed at some

grain boundaries, and authors have determined that this is due to the misorientation angle dependence. Similarly, HC CoCrMo may have a threshold misorientation angle between grains at which the grain boundary is susceptible to preferential corrosion. This may be due to higher energies at grain boundaries with a higher misorientation angle. [19-21]
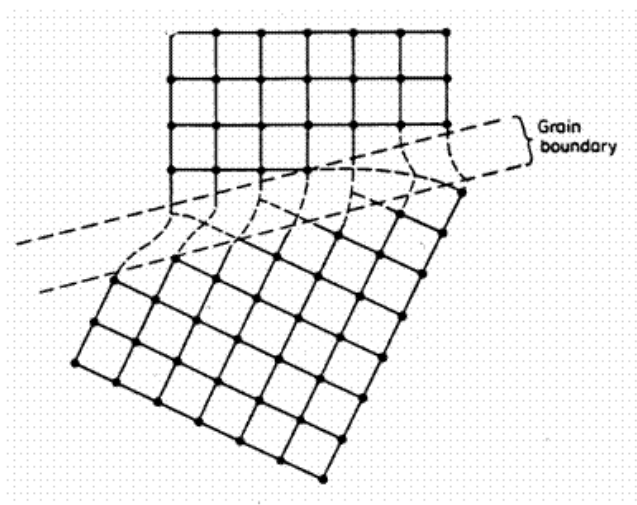
Figure 28. General structure of grain boundaries

For this reason, future work includes EBSD analysis of the HC CoCrMo surfaces after corrosion to verify if the misorientation angle is indeed correlated to the degree of grain boundary corrosion. EELS across the grain boundaries and phase boundaries will also be conducted to determine the degree of chromium depletion across the grain boundaries for the various solution anneals.

5 - Conclusions

Solution annealing CoCrMo results in a lower corrosion rate without affecting the passive film's properties as a kinetic barrier to corrosive processes. This lower corrosion rate is attributed to the effects of grain coarsening and second phase dissolution that occur upon annealing, since the grain and phase boundaries suffer more preferential corrosion. The grain boundaries which are not corroded are most likely due to a low misorientation

angle between the adjacent grains. These findings suggest that HC CoCrMo with coarser grains (and potentially even single-crystal CoCrMo) and dissolved second phases might be a superior materials choice for medical implants, as these may better resist corrosion.

6 - Acknowledgements

References

[1]   S. Pramanik, A. K. Agarwal, and K. N. Rai, "Chronology of Total Hip Joint Replacement and Materials Development," *Trends in Biomaterials and Artificial Organs,* vol. 19, pp. 15-26, 2005.

[2]   N. J. Hallab, R. M. Urban, and J. J. Jacobs. *Biomaterials in Orthopedics*.

[3]   M. M. Mikhael, A. D. Hanssen, and R. J. Sierra, "Failure of Metal-on-Metal Total Hip Arthroplasty Mimicking Hip Infection. A Report of Two Cases," *The Journal of Bone and Joint Surgery,* vol. 91, pp. 443-446, 2009.

[4]   N. Hallab, K. Merritt, and J. J. Jacobs, "Metal Sensitivity in Patients with Orthopaedic Implants," *The Journal of Bone and Joint Surgery,* vol. 83, 2001.

[5]   M. T. Mathew, C. V. Nagelli, M. J. Runa, R. Pourzal, A. Fischer, M. P. Laurent, J. J. Jacobs, and M. A. Wimmer, "Does the Tribolayer on a Metal-on-Metal (MoM) Hip Joint Exhibit Superior Corrosion Resistance?," Rush University Medical Center, Chicago, IL.

[6]   M. Caudillo, M. Herrera-Trejo, M. R. Castro, E. Ramirez, C. R. Gonzalez, and J. I. Juarez, "On Carbide Dissolution in an As-Cast ASTM F-75 Alloy," *Journal of Biomedical Materials Research,* vol. 59, pp. 378-385, 2002.

[7]   K. P. Gupta, "The Co-Cr-Mo (Cobalt-Chromium-Molybdenum) System," *Journal of Phase Equilibria and Diffusion,* vol. 26, pp. 87-92, 2005.

[8]   Y. Liao, R. Pourzal, P. Stemmer, M. A. Wimmer, J. J. Jacobs, A. Fischer, and L. D. Marks, unpublished|.

[9]   A. J. T. Clemow and B. L. Daniell, "Solution Treatment Behavior of Co-Cr-Mo Alloy," *Journal of Biomedical Materials Research,* vol. 13, pp. 265-279, 1979.

[10]   T. Kilner, R. M. Pilliar, G. C. Weatherly, and C. Allibert, "Phase Identification and Incipient Melting in a Cast Co-Cr Surgical Implant Alloy," *Journal of Biomedical Materials Research,* vol. 16, pp. 63-79, 1982.

[11]   "Standard Specification for Wrought Cobalt-28Chromium-6Molybdenum Alloys for Surgical Implants (UNS R31537, UNS R31538, and UNS R31539)," Designation F 1537-08, ed. West Conshohocken, PA: ASTM International, 2008.

[12]   C. V. Vidal and A. I. Munoz, "Study of the adsorption process of bovine serum albumin on passivated surfaces of CoCrMo biomedical alloy," *Electrochimica Acta,* vol. 55, pp. 8445-8452, 2010.

[13]   K. Rajan, "Thermodynamic Assessment of Heat Treatments for a Co-Cr-Mo Alloy," *Journal of Materials Science,* vol. 18, pp. 257-264, 1983.

[14]   Y. Yan, A. Neville, D. Dowson, and S. Williams, "Tribocorrosion in Implants - Assessing High Carbon and Low Carbon Co-Cr-Mo Alloys by In Situ Electrochemical Measurements," *Tribology International,* vol. 39, pp. 1509-1517, 2006.

[15]   R. T. Blunt, presented at the CS MANTECH Conference, Vancouver, British Columbia, Canada, 2006.

[16]   C. Montero-Ocampo and E. L. Martinez, "Effect of Carbon Content on the Electrochemical Impedance of As-Cast CoCrMo," *ECS Transactions,* vol. 19, p. 37, 2009.

[17]   Y. Sato, N. Nomura, S. Fukinuma, and A. Chiba, "Microstructure and Mechanical Properties of Hot-Pressed Co-Cr-Mo Alloy Compacts," *Advanced Materials Research,* vol. 26-28, pp. 769-772, 2007.

[18]   B. Valcu and H. N. Bertram, "Effect of Cr concentration gradient on the intergranular exchange in CoCr(Ta,Pt) thin films," *Journal of Applied Physics,* vol. 91, pp. 764-771, 2002.

[19]   L. H. Chan, H. Weiland, S. Cheong, G. S. Rohrer, and A. D. Rollett, unpublished|.

[20]   X. R. Qian, Y. T. Chou, and E. A. Kamenetzky, "The structure dependence of grain boundary corrosion in niobium bicrystals," *Journal of the Less Common Metals,* vol. 134, pp. 179-185, 1987.

[21]   Y. Yuan and A. J. Davenport, "Crystallographic effects in intergranular corrosion of an Al-Mg alloy," S. o. M. a. M. The University of Birmingham, Ed., ed. Adgbaston, Birmingham, UK, 2005